SCIENCE CHINA
Chemistry

•ARTICLES•
SPECIAL ISSUE: Dedicated to the 100th Anniversary of Nankai University

May 2019 Vol.62 No.5: 602–608
https://doi.org/10.1007/s11426-018-9370-0

Facile construction of two-dimensional coordination polymers with a well-designed redox-active organic linker for improved lithium ion battery performance

Jingwei Liu[1], Lin Zhang[1], Huanhuan Li[1], Peng Zhao[1], Peng Ren[2], Wei Shi[1*] & Peng Cheng[1,3*]

[1]*Key Laboratory of Advanced Energy Materials Chemistry of Ministry of Education, College of Chemistry, Nankai University, Tianjin 300071, China;*
[2]*School of Science, Harbin Institute of Technology (Shenzhen), Shenzhen 518055, China;*
[3]*Collaborative Innovation Center of Chemical Science and Engineering (Tianjin), Nankai University, Tianjin 300071, China*

Received August 22, 2018; accepted October 16, 2018; published online January 7, 2019

A well-designed redox-active organic linker, pyrazine-2,3,5,6-tetracarboxylate (H_4pztc) with brimming active sites for lithium ions storage was utilized to construct coordination polymers (CPs) via a facile hydrothermal reaction. Those two isostructural two-dimensional (2D) CPs, namely $[M_2(pztc)(H_2O)_6]_n$ (M=Co for **1** and Ni for **2**), delivered excellent reversible capacities and stable cycling performance as anodes in lithium ion batteries. As demonstrated in electrochemical studies, **1** and **2** can achieve highly reversible capacities of 815 and 536 mA h g^{-1} at 200 mA g^{-1} for 150 cycles, respectively, best performed for the reported 2D-CP-based anode materials. The electrochemical mechanism studies showed that the remarkable performances can be ascribed to the synergistic Li-storage redox reactions of metal centers and organic moieties. Our work highlights the opportunities of using a well-designed organic ligand to construct low-dimensional CPs as new type of electrode materials for advanced lithium ion batteries.

two-dimensional coordination polymers, anode materials, lithium ion battery

Citation: Liu J, Zhang L, Li H, Zhao P, Ren P, Shi W, Cheng P. Facile construction of two-dimensional coordination polymers with a well-designed redox-active organic linker for improved lithium ion battery performance. *Sci China Chem*, 2019, 62: 602–608, https://doi.org/10.1007/s11426-018-9370-0

1 Introduction

To satisfy the increasingly urgent demands for energy, enormous efforts have been made to exploit renewable and pollution-free resources [1,2]. Lithium ion batteries (LIBs) have become one of the most significant devices for electrical energy storage in consumer electronics and electric vehicles, owing to their high energy capacity, environmental compatibility, and no memory effect during cycling processes. However, the energy and power densities of LIBs can hardly fulfill the requirements for the large-scale electrical applications [3–5]. As a result, a wide range of functional materials including metal oxides/sulfides, carbon materials, metallic alloys have been exploited as alternatives to the traditional graphite anodes for improving electrochemical performance [6–8]. There is a lot of room to investigate anode materials with higher capacity, excellent rate capability and long cycling performance.

Coordination polymers (CPs) are crystalline materials composed of one-dimensional (1D), two-dimensional (2D), or three-dimensional (3D) ordered networks assembled by joining metal nodes with preferable organic linkers [9]. Metal-organic frameworks (MOFs) are subfamily of CPs, with the characteristic of porous structure [10]. Due to the inherent superiority of easy preparation with wide synthesis procedures, controllable porosities and structures, CPs and

*Corresponding authors (email: shiwei@nankai.edu.cn; pcheng@nankai.edu.cn)

MOFs have shown great performance in a variety of applications, such as gas storage and separation, drug delivery, chemical sensing and catalysis [11]. Recently, the applications of pristine MOFs, MOF-composites, and MOF-derived materials for energy storage and conversion are burgeoning [12]. In particular, pristine CPs and MOFs have been directly utilized as electrodes for the improvement of LIBs performance [13]. MOF-177 was initially investigated as anode materials of LIBs in 2006 [14]. Albeit the poor cycling stability and limited storage capacity, this pioneering work has boosted the constant discovery of CPs or MOFs as advanced anode materials for LIBs with superb electrochemical properties. After that, other MOFs, such as Mn-LCP, $Zn_3(HCOO)_6$, and Fe-MIL-88B have also been reported [15–17]. According to the previous studies, the electrochemical reaction mechanisms of lithiation/delithiation in CPs can be divided into two types. (1) Redox or conversion type: the redox involvement of metal ions and functional groups or atoms (carboxyl groups, anime groups and N atoms) of organic ligands [18]; (2) insertion type: Li-ions stored in the pores or the conjugated aromatic rings [12,19].

Inspired by the Li-storage mechanism studies, we choose pyrazine-2,3,5,6-tetracarboxylic acid (H_4pztc) as organic linker to construct CPs for high-performance LIBs. H_4pztc is an ideal ligand material with the features of brimming active sites for Li-ions storage, easy synthesis, and lower molecular weight. The functional groups and atoms (carboxyl groups and N atoms) of H_4pztc can reversibly store Li-ions by means of redox type. Lithium insertion/extraction in the conjugated aromatic ring can repeatedly occur during electrode reactions through insertion type. As a consequence, the construction of H_4pztc-based coordination polymers is a sensible strategy for anode materials of LIBs to pull the pristine MOFs-based anodes out of the current funk. The ligand was obtained according to the published procedure (Figure 1(a)) [20].

At present, numerous CPs as anode materials of LIBs have been extensively studied [13]. However, the framework structures of 3D CPs usually decompose accompanied by the reduction of metal ions during discharging, and the structures cannot recover after the recharge process. It has been proposed that reducing the dimensions and judicious selection of organic ligands are effective ways to develop advanced conversion-type and insertion-type CPs as anode materials of LIBs [21]. Inspired by the successful application of 2D materials (i.e., graphene, transition metal oxides, transition metal dichalcogenides) in the energy storage and conversion field because of their atomically thin structures and great diversities [22–24], we introduced two isostructural CPs $[M_2(pztc)(H_2O)_6]_n$ (M=Co for **1**, Ni for **2**) with 2D layered structures achieved by a simple hydrothermal reaction as anode materials for LIBs. As expected, CPs **1** and **2** showed highly reversible specific capacities of 815 and 536 mA h g^{-1} at 200 mA g^{-1} over 150 cycles, respectively. In particular, **2** exhibited the most exceptional Li-storage performance compared with the reported Ni-based MOF anodes [25–28]. Furthermore, the lithiation-delithiation chemistry investigation of CPs **1** and **2** was intensively studied by *ex-situ* X-ray photoelectron spectroscopy (XPS) technology, the results of which confirm that metal ions and organic moieties synergistically participate in the redox electrode reactions.

2 Experimental

2.1 Materials and method

All the reagents and solvents were of analytical grade without any purification, except for H_4pztc, which was synthesized following the published procedure [20]. Powder X-ray diffraction (PXRD) measurements were recorded on a Rigaku Ultima IV instrument (Japan) in the 2θ range of 5°–50° at the scanning rate of 0.2° s^{-1}. Elemental analyses (EA) of C, H and N were collected on a Vario EL cube elemental analyzer (Elementar, Germany). The thermal gravimetric analysis (TGA) experiments were carried out using a Labsys NETZSCH TG 209 Setaram apparatus (Germany) at the heating rate of 10 °C min^{-1} under nitrogen atmosphere. The Fourier transform infrared (FT-IR) spectra were obtained in the wavenumber range of 400–4000 cm^{-1} on a Bruker ALPHA-T infrared spectrophotometer (Germany). Scanning electron microscopy (SEM) images were measured by a ZEISS MERLIN compact (field emission) scanning electron microscope (Germany) operating at 5 kV, 100 μA. X-ray photoelectron spectroscopy (XPS) was recorded on a Kratos AXIS Ultra DLD spectrometer (UK) with an Al Kα X-ray source.

2.2 Synthesis of H_4pztc

A mixture of 2,3,5,6-tetramethylpyrazine (22.1 mmol, 3.00 g), potassium hydroxide (52.8 mmol, 2.96 g) was dissolved in water (250 mL). $KMnO_4$ powder was added to the mixture in batches, which was stirred for 6 h at 60 °C to complete the oxidization. After that, adequate amount of ethanol was dropped to the mixture and the filtrate was concentrated and acidified to acquire the white power. Then the oxidation products were recrystallized from 25 mL of 20% aq. HCl, yield 55%. ^{13}C NMR (400 MHz, D_2O): δ 167.53, 145.57.

2.3 Synthesis of CPs 1 and 2

A mixture of $Co(NO_3)_2$•$6H_2O$ (58 mg, 0.2 mmol), H_4pztc (25.8 mg, 0.1 mmol), H_2O (5 mL) was sealed in a 10 mL vial and heated at 80 °C for 48 h, and then slowly cooled to room temperature. Light yellow crystals of **1** were obtained as a pure phase and rinsed with water and ethanol three times,

followed by vacuum desiccation at room temperature overnight. **2** was synthesized in the same way as **1** by changing $Co(NO_3)_2$•$6H_2O$ to $Ni(NO_3)_2$•$6H_2O$ (58 mg, 0.2 mmol). Elemental analysis calcd (%) for $C_4H_6CoNO_7$: C 20.10, H 2.53, N 5.86; found: C 19.96, H 2.47, N 6.01. Elemental analysis calcd (%) for $C_4H_6NiNO_7$: C 20.12, H 2.53; found: C 19.78, H 2.86, N 6.12. In FT-IR spectra (Figure S1, Supporting Information online), the positions and strength of the peaks are basically the same for the two isostructural metal-organic materials.

2.4 X-ray crystallography

The crystal structure of **1** was acquired by an Agilent Technologies Supernova single-crystal X-ray diffractometer (USA) using graphite-monochromatic Mo Kα radiation (λ= 0.71073 Å) at 120 K. The structure was solved with direct methods using SHELXS program and refined with full-matrix least-squares techniques on F^2 using SHELXL in the Olex2 software packages [29]. All the hydrogen atoms on the organic ligands were calculated geometrically and refined by riding model [30,31]. The crystallographic data and structure refinement parameters are summarized in the Table S1 (Supporting Information online).

2.5 Lithium ion battery fabrication

Standard CR2032 coin-type half-cells were assembled in an argon-filled glovebox to investigate the lithiation/delithiation behaviors of the prepared anodes. A homogenous slurry was acquired by mixing the electrode-active materials with Ketjen black and polyvinylidene fluoride (70:20:10 in weight) in *N*-methyl-2-pyrrolidone. The obtained slurry was cast on a copper foil and dried at 60 °C under a vacuum for 24 h in succession. The mass loading of a work electrode is about 1.2–1.6 mg cm^{-2}. For lithium ion battery fabrication, Li metal served as the counter/reference electrode. The composition of the electrolyte was 1 M $LiPF_6$ dissolved in ethylene carbonate (EC)/diethylcarbonate (DEC) (1:1, *v*/*v*). The separators of the cells were polypropylene film. The batteries were aged overnight before electrochemical tests. Galvanostatic charge-discharge tests were performed on a LAND battery tester in a temperature-controlled thermotank with the potential range of 0.01–3.0 V (vs. Li/Li^+) based on the weight of the active materials. Cyclic voltammetry (CV) and electrochemical impedance spectroscopy (EIS) measurements were performed on a CHI 660E electrochemical workstation (ChenHua Instruments Co., China).

3 Results and discussion

The crystal structure of **2** has been initially reported by Alfonso in 2001 [32]. Single-crystal X-ray diffraction analysis of **1** reveals that the two CPs are isostructurally crystallized in the triclinic space group $P\bar{1}$. CPs **1** and **2** are also characterized by FT-IR and PXRD measurements (Figures S1 and S2). The crystal structure of **1** is described as an example. There are two crystallographically independent Co^{2+} ions located in two types of distorted octahedral environments (Figure 1(b)). Co1 is connected with four H_2O molecules and two carboxyl oxygen atoms from two $pztc^{4-}$ anions. The coordination environment of Co2 is completed by two carboxyl oxygen atoms and two nitrogen atoms from two $pztc^{4-}$ anions, in addition to two oxygen atoms from two H_2O molecules (Figure 1(c)). The Co–O bond lengths vary from 2.056(6) to 2.116(8) Å, and the Co–N bond distance is 2.176(7) Å (Table S2). Each $pztc^{4-}$ anion serves as a linker and connected with four Co^{II} ions via N and O atoms to afford a 2D network structure (Figure 1(d)). The adjacent 2D layers are connected by hydrogen bonds of O6–H6A···O2, O7–H7A···O6 and O7–H7B···O1 (Table S3) from coordinated water molecules and carboxyl groups of $pztc^{4-}$ anions to form a 3D supramolecular framework (Figure 1(e)).

For the application of CPs as electrode materials for LIBs, high chemical stability of CPs in the electrolyte is crucial. Fortunately, the formation of the 2D planes linked by hydrogen bonds can increase the chemical and structural durability of both CPs in the electrolyte. These active materials maintain crystallinity after soaked in the electrolyte of LIBs for 7 d (Figure S3), which is confirmed by PXRD and FT-IR measurements (Figures S2 and S4). PXRD patterns of the obtained CPs **1** and **2** are in agreement with the simulated patterns based on the single-crystal data, confirming a pure solid-state phase (Figure S2). The TGA of CPs **1** and **2** were

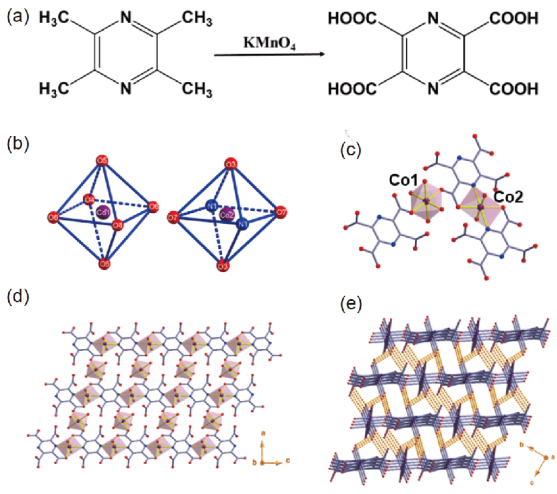

Figure 1 (a) Synthesis of H_4pztc; (b) coordination geometries of Co^{II} ions in **1**; (c) the coordination environments in **1** (hydrogen atoms were omitted for clarity); (d) wavy layers along the *b* axis; (e) the 3D supramolecular structure of **1** along the *a* axis. Atom colors: Co (purple), C (gray), N (blue), and O (red) (color online).

measured in the temperature range of 40–800 °C (Figure S5). **1** shows a weight loss of 22.36% from 80 to 305 °C and that of **2** is 22.38% from 95 to 312 °C, corresponding to the release of six coordinated water molecules (calcd 22.59% for **1** and 22.61% for **2**). Further heating generated rapid weight losses, indicating the collapse of the frameworks. The results indicate that the CPs display good crystalline phases and relatively high thermal stabilities.

To evaluate the redox activities of H_4pztc and H_4pztc based metal-organic materials, the energy levels of the lowest unoccupied molecular orbital (LUMO) and the highest occupied molecular orbital (HOMO) were calculated using density functional theory (DFT) [33,34]. The deeper LUMO is, the higher electron affinity (EA) and oxidizability exhibits. As shown in Figure 2, the LUMO of **1** (−5.52 eV) and **2** (−4.16 eV) are lower than that of H_4pztc (−3.15 eV). Besides, the energy gaps (ΔE) between the LUMO and HOMO levels are relevant to the intrinsic electrochemical activities, and a lower gap represents better activity [35,36]. On account of the coordination interaction between H_4pztc and the metal ions, the energy gaps of **1** (0.81 eV) and **2** (0.32 eV) are much lower than that of H_4pztc (4.75 eV), indicating that the intrinsic electrochemical activities in CPs **1** and **2** are higher than that for H_4pztc.

The electrochemical performances of the two isostructural CPs as LIBs anode materials were evaluated in a voltage window of 0.01–3.0 V (vs. Li/Li^+). Figure 3(a, b) shows the charge-discharge profiles of selected individual cycles at a representative current density of 200 mA g^{-1}. The electrode with **1** presents a meaningfully lower discharge plateau in comparison to that of **2**, indicating a more advantageous anodic characteristic. For **1**, the initial discharge and charge capacity are 2165 and 1107 mA h g^{-1}, respectively, with an initial Coulombic efficiency (ICE) of 51.1%. The initial irreversible capacity loss is attributed to the irreversible processes, including the decomposition of the electrolyte to form solid electrolyte interphase (SEI) layers and interfacial lithium storage [37,38]. Besides, the formation of Li_2O inside the interlayers or on the surface caused by the reaction between coordinated water molecules in **1** and lithium leads to the reversible capacities decay from the second cycle to the 10th cycle [39,40]. The ICE of **2** is only 47.3%, and then the CE maintains steady at nearly 100% in the following cycles, indicating that the SEI layers are stable.

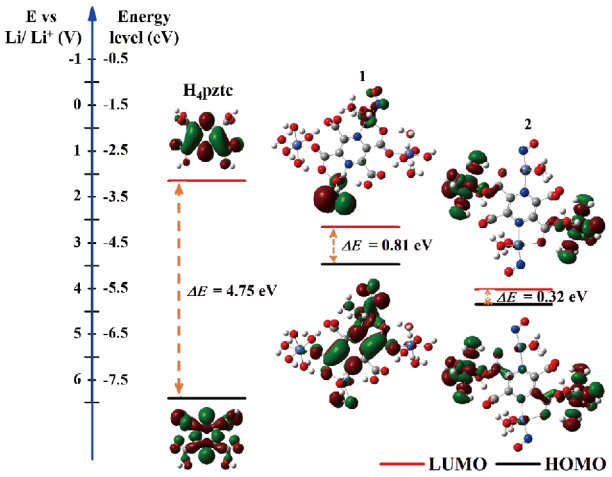

Figure 2 Calculation of the relative energies and spatial distributions of HOMO and LUMO energy levels for H_4pztc, **1**, and **2**. The left axis represents the relative energy voltage (vs. Li/Li^+, E_{Li/Li^+}) and the right axis represents the relative energy level in vacuum (E_{vac}) (color online).

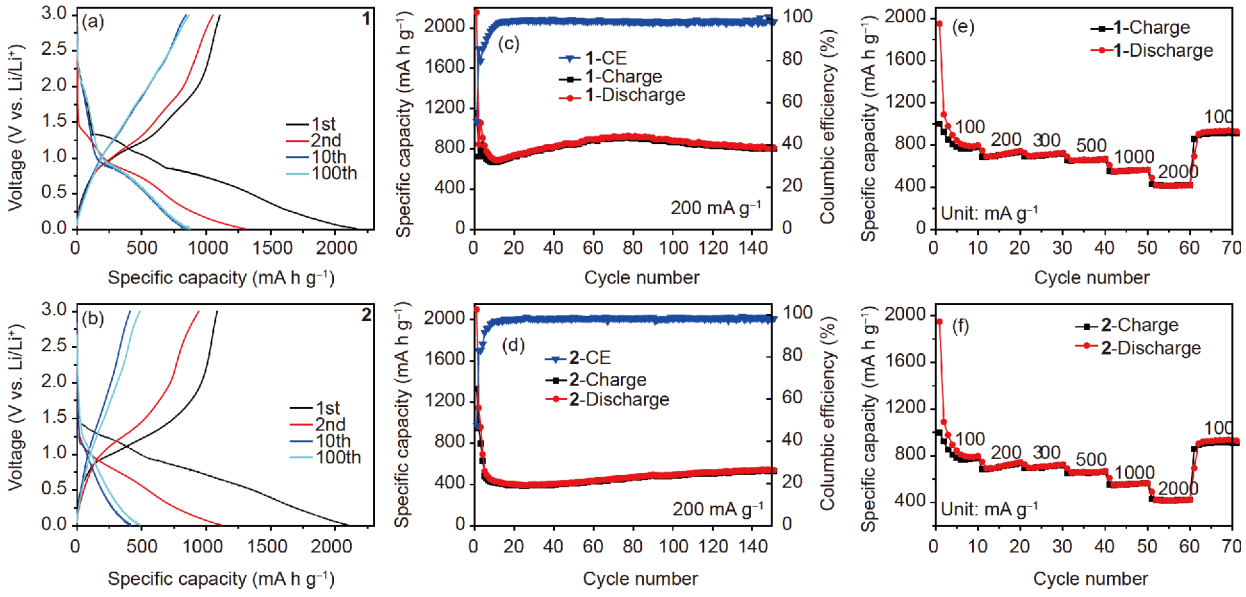

Figure 3 Electrochemical performances of two CPs as LIBs anodes: charge-discharge profiles at 200 mA g^{-1} of the **1** (a) and the **2** (b); cycling performances of **1** (c) and **2** (d) at 200 mA g^{-1} over 150 cycles; rate performance of **1** (e) and **2** (f) at different current densities (color online).

The cycling performances of the two CP-based anodes were investigated at 200 mA g^{-1}. As shown in Figure 3(c, d), the two CPs exhibited remarkable cycling stability with high reversible capacity. After 150 cycles, the discharge capacities of CPs **1** and **2** still retain at 815 and 536 mA h g^{-1} with relatively high capacity retention, which are higher than the theoretical capacity of commonly used graphite (372 mA h g^{-1}). After the specific capacities decrease for the first 10 cycles caused by the formation of Li_2O, the capacities of electrodes increase from the 10th to the 80th cycle and then maintain stable up to 150 cycles. This phenomenon of the capacities increasing should be related to the gradually electrochemical activation of the SEI film accompanied by better Li-diffusion kinetics during cycling [41], which was also observed in other CPs or MOFs [17,27,42]. When performed at 500 mA g^{-1}, the reversible capacities of CPs **1** and **2** are 615 and 410 mA h g^{-1} after 400 cycles, respectively (Figure S6(a, b)). The rate performances of the electrodes are illustrated in Figure 3(e, f). When the rates are gradually changed from 100 to 200, 300, 500, 1000 and 2000 mA g^{-1}, the corresponding discharge capacities are 845, 743, 698, 656, 558 mA h g^{-1} for **1** and 668, 483, 420, 365, 273, 211 mA h g^{-1} for **2**, respectively. When the current rate is reduced back to 100 mA g^{-1}, the reversible capacities swiftly recover to the initial stage without apparent decay, demonstrating the excellent cycling stability to tolerate the current change. In comparison with the organic ligand H_4pztc (Figure S7) and other pristine CPs as anode materials (Table S4), the two isostructural CPs in this work possess high reversible capacity and excellent electrochemical cycling stability and outperform all the reported 2D-CP-based anode materials.

To investigate the electrochemical redox reaction mechanism, cyclic voltammetry (CV) measurement was performed first. As shown in Figure S8, in the first cycle, the CV curves are different from the subsequent cycles, which can be related to the formation of SEI layers in both CPs **1** and **2**. In the subsequent scans, two apparent catholic peaks at 0.68 and 1.30 V, as well as two anodic peaks at 1.49 and 1.92 V are observed for **1** (Figure 4(a)), coinciding well with the galvanostatic charge-discharge profiles. The former pair of redox peaks can be clearly attributed to the redox process between Co^{2+} and Co^0, while the latter redox peaks result from lithiation and delithiation of the carboxylate groups [43]. For **2**, a reversible delithiation potential was remained at 1.47 V (Figure 4(b)). Lithiation process took place at 0.61 and 1.28 V, indicating that similar two-step redox reactions as that in **1** are happening during the discharging process.

The results of CV and galvanostatic charge-discharge measurements have demonstrated the two-step lithiation/delithiation redox processes in the metal centres and carbonyl groups. To further confirm the electrochemical reaction mechanism, we tracked the change of valence and chemical bonding state of electrode materials during discharging/charging processes by *ex-situ* XPS experiments. The two typical characteristic peaks at 781.3 and 797.2 eV correspond to Co $2p_{1/2}$ and Co $2p_{3/2}$ in Co^{2+}; the two main peaks at 856.4 and 873.6 eV can be assigned to Ni $2p_{1/2}$ and Ni $2p_{3/2}$ in Ni^{2+} (Figure 4(c, d)). The signals at 785.1, 801.7 eV, for Co 2p, and 860.9 and 879.5 eV for Ni 2p are satellite peaks. After being fully discharged, the characteristic Co 2p peaks shift toward 778.3 and 793.0 eV and the characteristic Ni 2p peaks shift toward 852.2 and 870.1 eV, confirming the existence of Co^0 and Ni^0 (Figure 4(e, f)) [44]. The C 1s and O 1s spectra were also investigated to study the redox involvement of the organic ligand during lithiation-delithiation processes (Figures S9 and S10). The C 1s and O 1s spectra peak shifts and conversions of CPs **1** and **2** are analogous on account of the identical organic moieties. The C1s spectra after Li-ions insertion process can be divided into three peaks at (Figure S9(c, d)), i.e., 284.6 eV for the C=C bond of the pyrazine ring, 285.9 eV for carboxyl groups, and 289.8 eV for C–C bond of the enol structures, respectively [45]. The results indicate that the carboxyl groups of $pztc^{4-}$ transformed into the enol structures after discharging process. In the O 1s spectra of the discharged electrodes (Figure S10(c, d)), the peaks at 529.6 (or 529.4) and 531.1 eV are attributed to the lattice oxygen and the Li–O bond [46]. In addition, theoretical studies and electron paramagnetic resonance (EPR) measurements have concluded that the N atoms on the aromatic ring can participate in the electrochemical redox reaction during cycling [18,19], as observed in the Zn-ODCP electrode [47], N-COFs [48] and NNU-11 [49] electrodes. Based on the above observations and discussions, the remarkable LIBs performances of two CPs are achieved by the synergistic Li-storage reactions of metal ions and organic linkers (Figure S11).

But obviously, the electrochemical performance of **1** is much better than that of **2**, which could be ascribed to the coordination affinity difference to organic ligands as well as the electrochemical property of the metal ions [50]. The performance inferiority of **2** over **1** could result from the following reasons: (1) Ni^{2+} has a larger ion radius than Co^{2+}, leading to stronger steric hindrance in **2** toward Li-ions; (2) the Li-ions migration kinetics of **2** after 150 discharge-charge cycles is lower than that of **1** (Figures S12 and S13); (3) the calculated *b*-values of the anodic and cathodic peaks for **2** (0.56, 0.61) indicate a relatively weak surface-controlled capacitive contribution to total capacity when compared with **1** (Figure S14).

Structural stability is a significant characteristic of CPs or MOFs as electrode materials during the electrochemical reactions. SEM, PXRD and FT-IR measurements were conducted to analyse the chemical and structural durability of the active materials after the cycling test. From the SEM images, PXRD patterns and FT-IR spectra, the active materials after 10 cycles can maintain chemical and structural

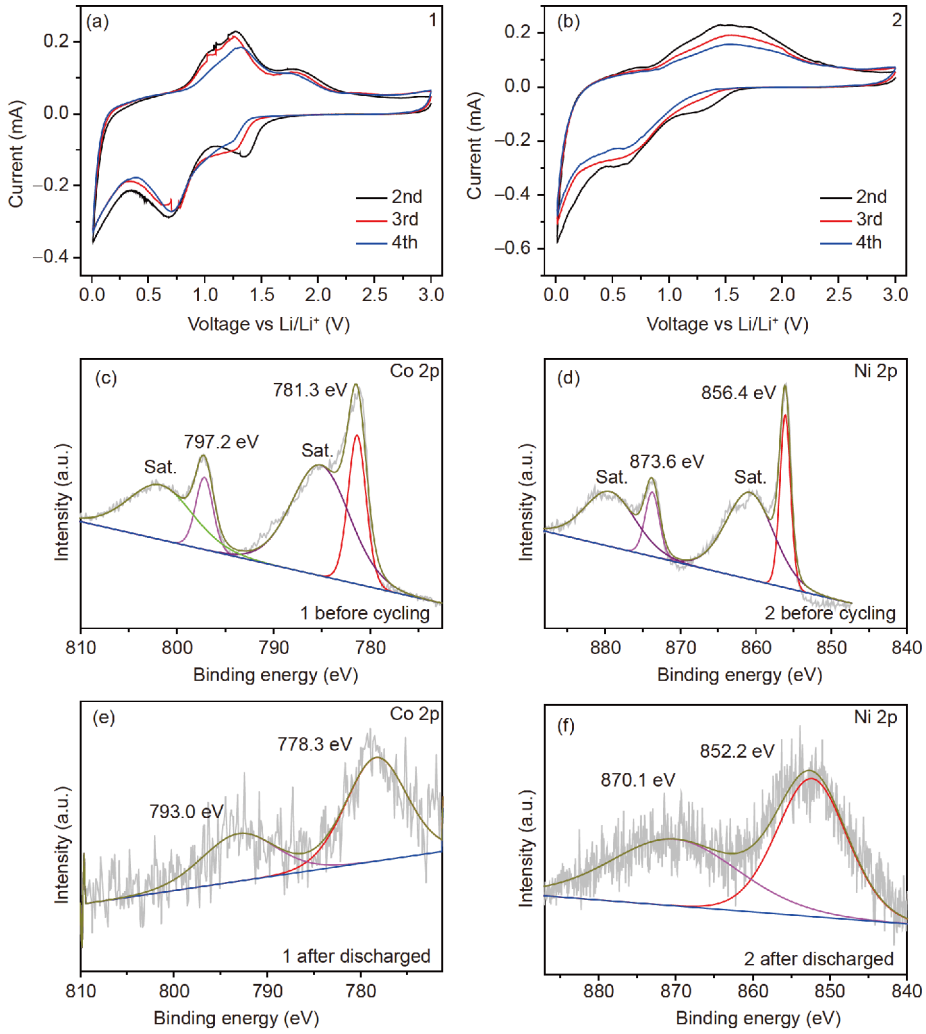

Figure 4 Cyclic voltammetry (CV) curves for the 2–4 cycles of **1** (a) and **2** (b) at a scan rate of 0.1 mV s^{-1} in the voltage window of 0.01–3.0 V vs. Li/Li^+. XPS spectra of **1** and **2** from the assembled electrodes before (c and d) and after (e and f) the electrochemical discharge processes (color online).

stabilities compared to that of the pristine CPs (Figures S15–S17). Besides, the morphologies of the assembled electrode materials can be well retained after 100 cycles at 500 mA g^{-1} (Figure S18). The results indicate that the 2D layer-based supramolecular structures can effectively tolerate the volume effects during charge and discharge processes, thereby, in favour of their long cycling performance.

4 Conclusions

In summary, we proposed a strategy of utilizing a well-designed redox-active organic ligand to construct 2D CPs for Li-storage for the first time. Two isostructural H_4pztc-based 2D layered CPs were obtained by a simple hydrothermal reaction. Both CPs exhibited highly reversible capacities and excellent rate performance, higher than any of the reported 2D-CP-based anode materials, to the best of our knowledge. The remarkable electrochemical properties are mainly ascribed to the synergistic Li-storage redox reactions of metal ions and organic moieties. In comparison with 3D CPs, the 2D layered CPs can effectively tolerate the volume effects during electrode reactions and facilitate Li-ions diffusion as well as electron transfer, which could further contribute to the improved LIBs performance. The present study may open a new avenue for the design and construction of low-dimensional (1D, 2D) CPs with a delicate designed organic ligand of multi-electron redox property for energy storage and conversion.

Acknowledgements This work was supported by the National Natural Science Foundation of China (21622105, 21501071, 21421001), Shenzhen Fundamental Research Project (JCYJ20160525164227350), the Ministry of Education of China (B12015), and the Natural Science Foundation of Tianjin (18JCJQJC47200).

Conflict of interest The authors declare that they have no conflict of interest.

Supporting information The supporting information is available online at http://chem.scichina.com and http://link.springer.com/journal/11426. The supporting materials are published as submitted, without typesetting or

editing. The responsibility for scientific accuracy and content remains entirely with the authors.

1 Melot BC, Tarascon JM. *Acc Chem Res*, 2013, 46: 1226–1238
2 Tarascon JM, Armand M. *Nature*, 2001, 414: 359–367
3 Meng J, Guo H, Niu C, Zhao Y, Xu L, Li Q, Mai L. *Joule*, 2017, 1: 522–547
4 Liu Y, Zhou G, Liu K, Cui Y. *Acc Chem Res*, 2017, 50: 2895–2905
5 Assat G, Tarascon JM. *Nat Energy*, 2018, 3: 373–386
6 Muraliganth T, Vadivel Murugan A, Manthiram A. *Chem Commun*, 2009, 9: 7360–7362
7 Li X, Zheng S, Jin L, Li Y, Geng P, Xue H, Pang H, Xu Q. *Adv Energy Mater*, 2018, 8: 1800716
8 Gao M, Liu X, Yang H, Yu Y. *Sci China Chem*, 2018, 61: 1151–1158
9 Chen B, Xiang S, Qian G. *Acc Chem Res*, 2010, 43: 1115–1124
10 Zhou HC, Long JR, Yaghi OM. *Chem Rev*, 2012, 112: 673–674
11 Furukawa H, Cordova KE, O'Keeffe M, Yaghi OM. *Science*, 2013, 341: 1230444
12 Wang L, Han Y, Feng X, Zhou J, Qi P, Wang B. *Coord Chem Rev*, 2016, 307: 361–381
13 Zheng S, Li X, Yan B, Hu Q, Xu Y, Xiao X, Xue H, Pang H. *Adv Energy Mater*, 2017, 7: 1602733
14 Li X, Cheng F, Zhang S, Chen J. *J Power Sources*, 2006, 160: 542–547
15 Liu Q, Yu L, Wang Y, Ji Y, Horvat J, Cheng ML, Jia X, Wang G. *Inorg Chem*, 2013, 52: 2817–2822
16 Saravanan K, Nagarathinam M, Balaya P, Vittal JJ. *J Mater Chem*, 2010, 20: 8329–8335
17 Shen L, Song H, Wang C. *Electrochim Acta*, 2017, 235: 595–603
18 Li G, Yang H, Li F, Cheng F, Shi W, Chen J, Cheng P. *Inorg Chem*, 2016, 55: 4935–4940
19 Lin Y, Zhang Q, Zhao C, Li H, Kong C, Shen C, Chen L. *Chem Commun*, 2015, 51: 697–699
20 Wolff L, Dtsch Ber. *Chem Ges*, 1887, 20: 425–433
21 Liang Z, Qu C, Guo W, Zou R, Xu Q. *Adv Mater*, 2018, 30: 1702891
22 Cong L, Xie H, Li J. *Adv Energy Mater*, 2017, 7: 1601906
23 Li X, Tao L, Chen Z, Fang H, Li X, Wang X, Xu JB, Zhu H. *Appl Phys Rev*, 2017, 4: 021306
24 Shi L, Zhao T. *J Mater Chem A*, 2017, 5: 3735–3758
25 An T, Wang Y, Tang J, Wang Y, Zhang L, Zheng G. *J Colloid Interface Sci*, 2015, 445: 320–325
26 Han X, Yi F, Sun T, Sun J. *Electrochem Commun*, 2012, 25: 136–139
27 Li C, Hu X, Tong W, Yan W, Lou X, Shen M, Hu B. *ACS Appl Mater Interfaces*, 2017, 9: 29829–29838
28 Zhang Y, Niu YB, Liu T, Li YT, Wang MQ, Hou J, Xu M. *Mater Lett*, 2015, 161: 712–715
29 Sheldrick GM. SHELXTL NT Version 5.1. Program for Solution and Refinement of Crystal Structures. Germany: University of Göttingen, 1997
30 Sheldrick GM. *Acta Crystlogr A Found Crystlogr*, 2008, 64: 112–122
31 Dolomanov OV, Bourhis LJ, Gildea RJ, Howard JAK, Puschmann H. *J Appl Crystlogr*, 2009, 42: 339–341
32 Alfonso M, Neels A, Stoeckli-Evans H. *Acta Crystlogr C Cryst Struct Commun*, 2001, 57: 1144–1146
33 Peng C, Ning GH, Su J, Zhong G, Tang W, Tian B, Su C, Yu D, Zu L, Yang J, Ng MF, Hu YS, Yang Y, Armand M, Loh KP. *Nat Energy*, 2017, 2: 17074
34 Lou X, Ning Y, Li C, Shen M, Hu B, Hu X, Hu B. *Inorg Chem*, 2018, 57: 3126–3132
35 Wang H, Yuan S, Si Z, Zhang X. *Energy Environ Sci*, 2015, 8: 3160–3165
36 Deng Q, Fan C, Wang L, Cao B, Jin Y, Che CM, Li J. *Electrochim Acta*, 2016, 222: 1086–1093
37 Senthil Kumar R, Nithya C, Gopukumar S, Anbu Kulandainathan M. *Energy Tech*, 2014, 2: 921–927
38 Qin J, He C, Zhao N, Wang Z, Shi C, Liu EZ, Li J. *ACS Nano*, 2014, 8: 1728–1738
39 Torardi CC, Miao CR. *Chem Mater*, 2002, 14: 4430–4433
40 Gao S, Chen Z, Wei M, Wei K, Zhou H. *Electrochim Acta*, 2009, 54: 1115–1118
41 Wang J, Yang N, Tang H, Dong Z, Jin Q, Yang M, Kisailus D, Zhao H, Tang Z, Wang D. *Angew Chem*, 2013, 125: 6545–6548
42 Maiti S, Pramanik A, Manju U, Mahanty S. *ACS Appl Mater Interfaces*, 2016, 7: 16357–16363
43 Song H, Shen L, Wang J, Wang C. *J Mater Chem A*, 2016, 4: 15411–15419
44 Wagner CD, Riggs WM, Davis LE, Moulder JF, Muilenberg GE. *Handbook of X-ray Photoelectron Spectroscopy*. Eden Prairie: Perkin-Elmer Corporation, 1979
45 Beamson G, Briggs D. *High Resolution XPS of Organic Polymers: the Scienta ESCA300 Database*. Chichester: Wiley, 1992
46 Marco JF, Gancedo JR, Gracia M, Gautier JL, Ríos E, Berry FJ. *J Solid State Chem*, 2000, 153: 74–81
47 Song Y, Yu L, Gao Y, Shi C, Cheng M, Wang X, Liu HJ, Liu Q. *Inorg Chem*, 2017, 56: 11603–11609
48 Bai L, Gao Q, Zhao Y. *J Mater Chem A*, 2017, 4: 14106–14110
49 Huang Q, Wei T, Zhang M, Dong LZ, Zhang AM, Li SL, Liu WJ, Liu J, Lan YQ. *J Mater Chem A*, 2017, 5: 8477–8483
50 Zhang L, Cheng F, Shi W, Chen J, Cheng P. *ACS Appl Mater Interfaces*, 2018, 10: 6398–6406